PULSED LASER IRRADIATION FOR DISCRETE COMPONENT DOSE-RATE MODEL DEVELOPMENT

By

Sarah Armstrong Nation

Thesis

Submitted to the Faculty of the

Graduate School of Vanderbilt University

in partial fulfillment of the requirements

for the degree of

MASTER OF SCIENCE

in

Electrical Engineering

December, 2007

Nashville, Tennessee

Approved:

Professor Lloyd W. Massengill

Professor Michael Alles

ACKNOWLEDGEMENTS

I would like to express my gratitude to my advisor, Dr. Lloyd Massengill, for providing his technical expertise, guidance and patience throughout this endeavor (and beyond). I am grateful for the time spent in office hours, and finally, for the challenge to complete this project “on time”.

I very much appreciate the continued help and support of Dr. Dale McMorrow throughout this project (which would still be on the drawing board without his time and efforts). Also, I give my gratitude to Dr. Michael Alles for volunteering to review this manuscript and for his careful reading and valuable feedback. Lydell Evans receives my many thanks for his support and generous help with testing and for a demonstration of how an efficient LINAC test is run.

Thanks to my family for always supporting and believing in me, and for forgiving me for a short Thanksgiving this year. I am grateful to the members of my “support staff,” who remind me frequently of “the way things are.”

Finally, thanks to the management of NAVSEA Crane and the Naval Research Laboratory for providing the many resources that made this research possible and to the Radiation Effects Research Group and the faculty of the Department of Electrical Engineering and Computer Science at Vanderbilt University for continued technical support and productive feedback.

TABLE OF CONTENTS

Chapter **Page**

ACKNOWLEGEMENTS ii

LIST OF TABLES iv

LIST OF FIGURES v

I. INTRODUCTION 1

II. BACKGROUND 4

Weapons Environment 4
Device Effects 4
Device Modeling 6
Assertion of Work 10

III. TEST SETUP 12

Devices 12
LINAC Testing 13
Laser Testing 17

IV. RESULTS 21

Conversion Factor and Combined Results 21
Accounting for Metallization Coverage 28
Case Study of the 2N4391 34

V. CONCLUSIONS 37

REFERENCES 39

LIST OF TABLES

4-1 Summary of CF data 25

4-2 K_{pp} device values extracted from laser and LINAC data. 26

4-3 Percent metal coverage results of thresholding technique and summary of conversion factors. 30

LIST OF FIGURES

Figure **Page**

2-1 Dose-rate effects on a P-N junction [4]. 5

2-2 Photocurrent vs. dose rate for various device types [4]. 6

2-3 Gummel–Poon model topography including photocurrent generators [3]. 7

2-4 Sample cross-section for a version of the 2N2222 device used for extracting values for K_{pp} for dose-rate models. 8

2-5 I_{pp} vs. dose rate for the 2N4391 (JFET) device. 9

3-1 Schematic of device test board. 13

3-2 Photograph of LINAC 40 Pin I/O test fixture including lead bricks, and collimator. 14

3-3 Monitor diode response of typical LINAC pulse at 1.9 x 10^9 rad(si)/sec 15

3-4 Resulting photocurrent transient responses from the LINAC for each of the devices 16

3-5 Generated LINAC transients for PIN diode and photocurrent result 17

3-6 Diagram of Laser Setup 18

3-7 Monitor diode response of typical laser pulse 19

3-8 Resulting photocurrent transient responses from laser testing for each of the devices 20

4-1 LINAC I_{pp} vs. dose rate for each of the tested device types 22

4-2 Laser I_{pp} vs. dose rate for each of the four tested device types plotted vs. pulse energy (a) and I_{pp} vs. dose rate (b) 23

4-3 CF extraction procedure 24

4-4 Device-type relationship shift when CF is applied. All laser I_{pp} vs. laser energy data (a) and I_{pp} vs. dose rate laser data (b) 27

4-5 Combined LINAC and laser I_{pp} data 28

4-6 Laser irradiation and shadowing of a typical bipolar transistor cross section[11]....................29

4-7 Thresholding technique progression for the 2N2222A....................31

4-8 Conversion factor vs. percent metal coverage....................32

4-9 Geometry family groupings....................33

4-10 Establishment of geomentry family for the 2N4391....................35

4-11 Process flow using the 2N4391....................36

CHAPTER I

INTRODUCTION

Increased desktop computing power and the advancement of simulation tools enables accurate modeling of the radiation effects of different environments. Such modeling (and simulation) is useful in the design of integrated circuits and circuit boards for radiation environments. Designers of space and weapons systems look to exploit this computing power throughout the design process, from integrated circuit (IC) design to a full system simulation. In order to provide a complete library of radiation effects models, it is necessary to include base electrical and all the relevant radiation effects models for each device used in a specific application. Decisions as to what parts will be used in a system often are not solidified until well into the design cycle, necessitating a very quick response from those who are tasked to create the models. This is made more difficult because of financial and logistical issues with parts procurement and the availability of necessary model development information, either from manufacturers or from a test facility.

Discrete components are an often overlooked, yet essential part of modern system design. Board designers incorporate ICs and discrete parts to meet the design specifications. It is often the case that ICs are custom designed for the system, providing some initial design flexibility, but when the IC designs are finalized, the 'fine-tuning' of the circuit is done with discrete parts. This leads to a changing or growing discrete parts list and, therefore, an ever-evolving model development list.

Assuming parts and facilities are available, the data needed to create radiation effects models is relatively easy to extract. Total Ionizing Dose (TID) model information is extracted using a Co-60 source. These sources are readily available in many laboratory settings. Dose-rate, neutron, and heavy-ion testing require the use of special facilities such as linear accelerators (LINACs), flash x-rays (FXR), cyclotrons, and ion beams that are greatly limited in number and often require scheduling months in advance. This makes it difficult to accommodate last-minute changes to model development lists. This project proposes some lessening of the burden of LINAC and FXR facilities in their roles for dose-rate model development by providing a viable alternative for collecting the experimental data.

Equation-based "best guess" dose-rate models have been created for discrete components based on physical characteristics of the device [1-3] with good accuracy. These models are eventually verified using experimental data, traditionally obtained from LINAC or FXR testing. However, in an ideal situation, the necessary information for the photocurrent model is *extracted* from experimental data. While LINAC and FXR testing are invaluable for reliability and qualification testing, scheduling supplementary model testing during these critical periods can be difficult. In addition, data from these facilities can have low signal-to-noise ratios and a limited dynamic range compared to the desired range of model operation.

Previous work investigating laser dose-rate simulation indicates that a pulsed laser has the ability to effectively simulate the effects of pulsed radiation sources, but the quantitative calibration of the technique requires further exploration into the issues of metal coverage of the die, full illumination of the die, and beam profile. There are

current commercial applications for using a pulsed laser to simulate dose-rate effects, but these are limited to thresholding applications such as parts screening and trigger testing. These types of applications are generally tuned to a certain type of device and calibrated with LINAC data. The proposed technique involves the establishment of reference curves for devices classified by collection volume and will allow accurate dose-rate estimation for devices that fall within those classifications. The variable in this technique is the metallization coverage of the active area of the die.

This study explores further the possibilities of using a pulsed laser to create a clean, consistent set of data that will be useful to capture dose-rate model parameters. This work will illustrate that metallization coverage in discrete devices can be quantitatively accounted for in terms of a simple, linear conversion factor, effectively removing the primary limitation of a laser-based approach. A case-study is presented to demonstrate how this technique may be applied to extract the appropriate parameters to create a dose-rate model for a JFET device, which falls into the general collection volume classification that has been developed in this research.

CHAPTER II

BACKGROUND

Weapons Environment

The detonation of a nuclear weapon produces a broad spectrum of radiation effects including neutrons, x-rays, alpha, beta, and gamma radiation, and heavy ions [4]. This study focuses on the gamma-ray-induced effect. The primary shockwave of a detonation is a large burst of energy produced primarily by the gamma rays. From a weapons design viewpoint, it is necessary to design electronics that are able to detect a nuclear event and decide whether to attempt to operate through the event or shut down during the event. It is necessary to characterize the behavior of the electronics in a dose-rate environment to determine the suitability of electronics for the environment.

Device Effects

The fundamental theory of dose-rate effects can best be summarized using a P-N junction for illustration. Photocurrents are produced by the junction being exposed to high-energy radiation, producing electron-hole pairs in quantities that may exceed the doping levels of the device. Figure 2-1a shows a band diagram of a P-N junction "swamped" with excess majority carriers generated in the conduction and valence bands. These carriers are swept opposite the primary current flow, as seen in Figure 2-1b. The instantaneous value of this generated current, I_{pp}, is:

$$I_{pp} = g \cdot q \cdot A \cdot x \cdot \frac{d\gamma}{dt} \qquad (2.1)$$

In this equation, g is the generation rate (4.2×10^{13} pairs · cm^{-3} · $rad(Si)^{-1}$), q is the electron charge (C), A is the junction area (cm^2) , x is the depth of the collection region (cm), and $\frac{d\gamma}{dt}$ is the dose rate (rad(Si)/sec).

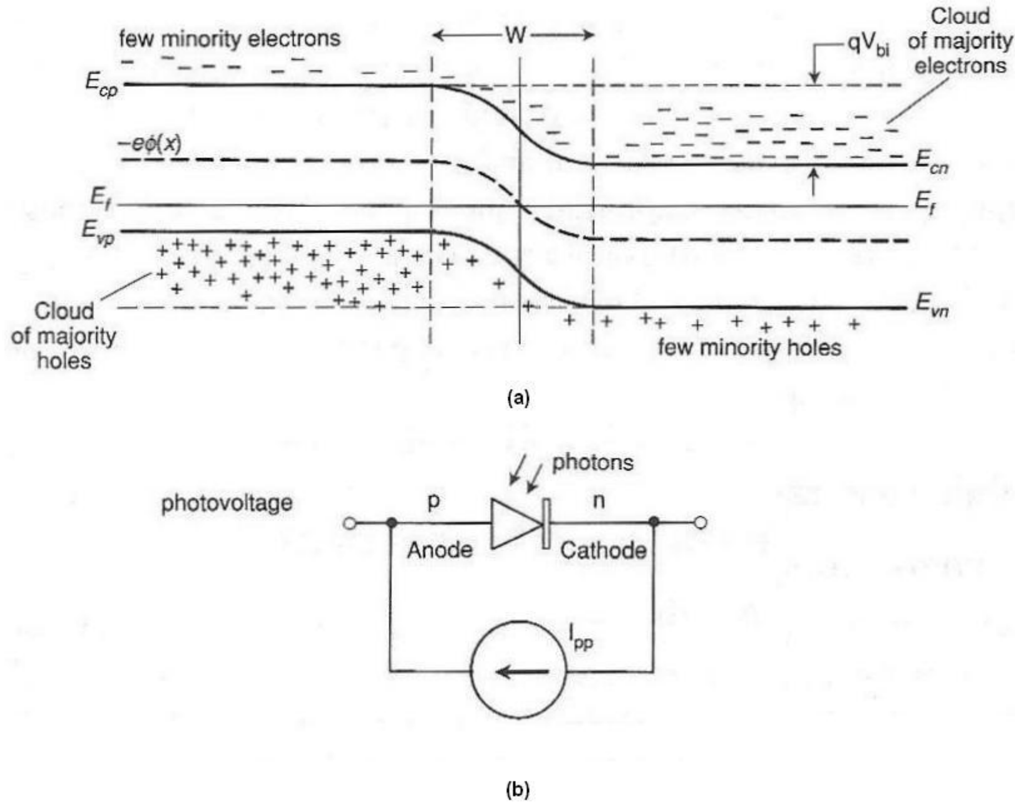

Figure 2-1: Dose-rate effects on an unbiased P-N junction. (a) High energy radiation generates majority carriers in the conduction and valence bands producing a current flow opposite the normal operation of the device. (b) Schematic representation of the generated current. Figure from Holmes-Seidle [4].

As can be seen in Equation 2.1, the generated photocurrent varies depending on the dimensions of the collection region and the excitation applied to the junction. Figure 2-2 shows idealized values for generated peak photocurrent, I_{pp}, for different silicon device families. As exposed area increases, so does the generated photocurrent.

This study focuses on the middle band of devices, the small-signal transistors and ICs. A subgroup of this class of devices is the bipolar junction transistors (BJTs), which will be the focus of the discussion of device modeling. It should be noted in Figure 2-2 that there is a discontinuity in the photocurrent vs. dose rate curve of interest to this study. This is caused by parasitic effects due to complex device geometries.

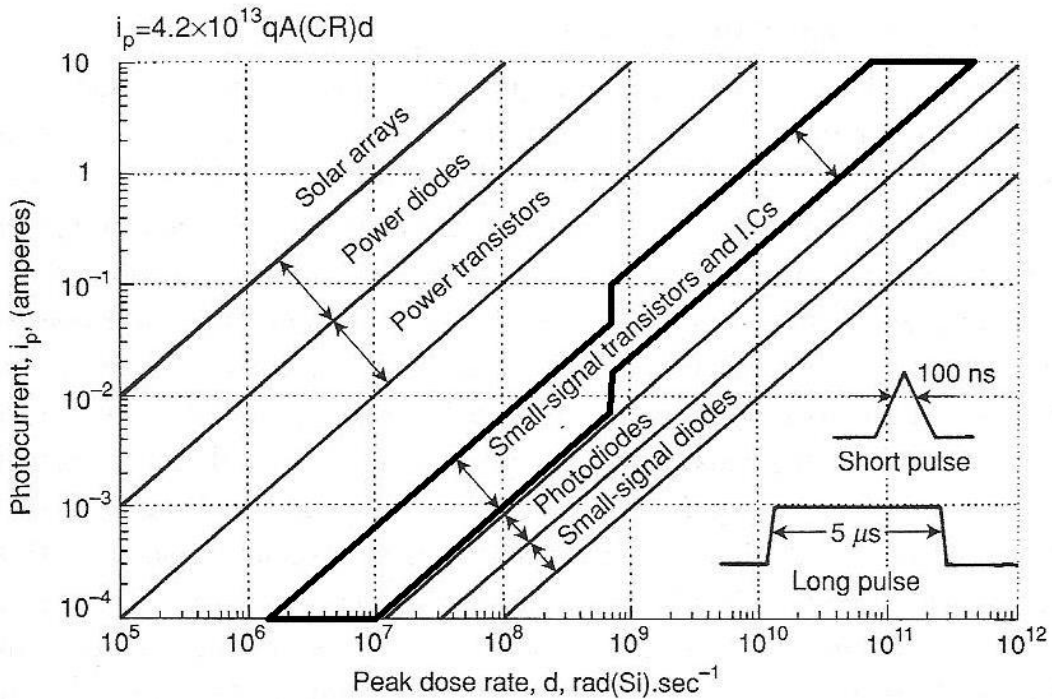

Figure 2-2: Photocurrent vs. dose rate for various device types. The bold outline highlights the area of interest for this research. Figure from Holmes-Seidle [4]

Device Modeling

A generally accepted technique for creating a dose-rate model for a bipolar transistor involves modifying a vendor-supplied electrical model by inserting current sources between the collector-base, emitter-base, and collector-substrate junctions, within the series resistances of the device [3]. Figure 2-3 shows a sample Gummel-Poon model

topology with these photocurrent generators.

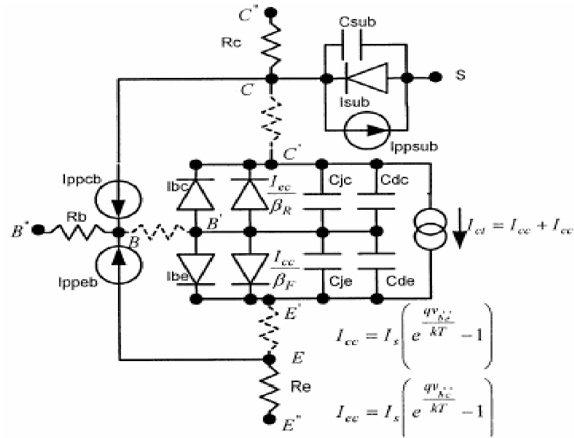

Figure 2-3: Gummel–Poon model topography including photocurrent generators. Figure from Alexander [3].

In practice, rather than inserting discrete values for I_{pp}, based on specific dose-rate values, a photocurrent-generating parameter, K_{pp} has been established as the slope of the I_{pp} vs. dose-rate curve. Referring to Figure 2-2, the slope of the lines for each of these devices would be the K_{pp} value. However, this value changes for each device type and is dependent primarily on the geometry of the specific device. This characteristic may be calculated as:

$$K_{pp} = g \cdot q \cdot A \cdot x \qquad (2.2)$$

In this equation the values are derived from physical characteristics and information from the manufacturer. Note that (2.2) is simply equation (2.1) without the dose rate multiplier.

It is obvious, then that:

$$I_{pp} = K_{pp} \cdot \frac{d\gamma}{dt} \qquad (2.3)$$

This geometrical information (active area, junction depth, etc.) is often difficult to obtain

directly from the manufacturer and device modelers often rely on reverse engineering via cross-section to provide a "best guess" estimate (see Figure 2-4).

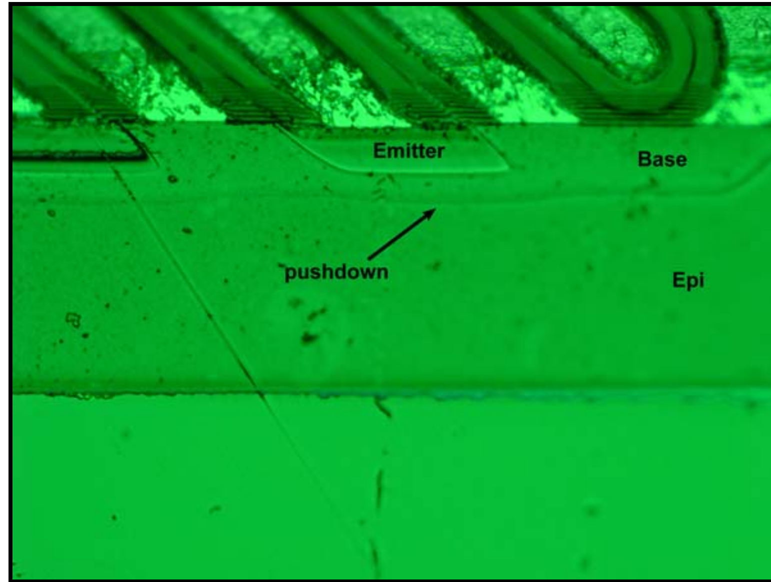

Figure 2-4: Sample cross-section for a version of the 2N2222 device used for extracting values for K_{pp} for dose-rate models. Photograph provided by NAVSEA Crane.

Ideally, the K_{pp} values of the devices are extracted from test data. Figure 2-5 shows a sample I_{pp} vs. dose-rate data set from which K_{pp} is derived from this slope of the linear region of the data. The linear portion of the data is typically determined visually. The non-linear portion, often described as the "roll-off", is illustrated in this figure. This phenomenon is caused by the internal collapse of the junction depletion region and intrinsic resistive effects, and is not addressed in this study. The selected linear data are used to extract a trendline via a standard graphing program. In this case, Microsoft Excel was used; Excel employs a least-squares fit for linear trendlines. The value for this specific device is indicated on the graph. This K_{pp} extraction technique is used throughout this work.

Whatever method is used to extract the K_{pp} value, either via device geometry or from test data, the value is inserted into the functional device model equations for the specific simulator. The K_{pp} value is used rather than a specific I_{pp} in order to provide the user flexibility to conveniently simulate a variety of dose rates. The radiation-enabled model must accept an input for a dose-rate value and the current source will simulate the appropriate peak current value using equation (2.3).

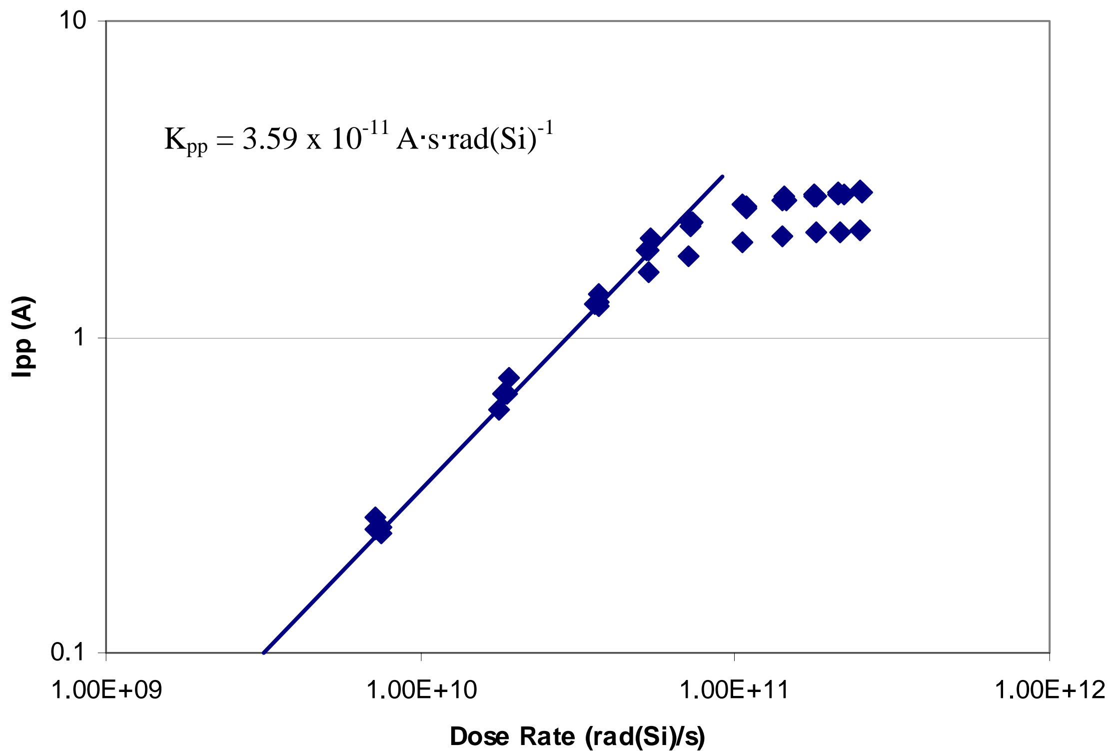

Figure 2-5: I_{pp} vs. dose rate for the 2N4391 (JFET). A best-fit line has been extracted for the linear portion of the data set (the remainder of the data is not factored into the determination of the linear fit). The slope of this line is K_{pp}. This figure is presented in context in Chapter IV.

It should be noted that employing the K_{pp} value to provide flexibility into the model leads to a linear extrapolation of the value of I_{pp} at dose-rates above the linear

region of the I_{pp} vs. dose-rate curve. For example, in Figure 2-5, the K_{pp} value at 2.5 x 10^{11} rad(Si)/sec yields an I_{pp} value of 9.0 A, while the collected data yields and I_{pp} value of only 2.18 A—a rather dramatic difference. The models described are acceptable for general application because they provide a "worst-case scenario" at the higher dose-rates and, as seen in this chapter, are relatively easy to derive from test data. More advanced dose-rate modeling techniques take the "roll-off" into account, but are significantly more time-intensive to derive.

Assertion of Work

The need to quickly create dose-rate models from test data for a flexible discrete parts list inspired this research. In the situation, test priority was appropriately assigned to evaluation and qualification testing at the available LINAC facility. Test data for the dose-rate models were eventually made available, but at a high cost in both materials and labor costs that could have been significantly lessened if an alternative to LINAC data collection had been available.

Laser testing to simulate dose rate events was first documented in the literature by Habing [5] who compared the photocurrent produced in isolated transistors by pulsed laser, flash x-ray, and LINAC. In his paper, Habing outlines the complications with dose rate laser testing such as extraction of the generation rate, accounting for metallization coverage, and methods of determining energy deposition. These topics are common discussion points when considering using a laser for dose rate simulation.

Other devices have been used to make similar comparisons through the years [6, 7], and other dose rate effects [8-10] and techniques [11-13] have been explored.

Overall, there has been good correlation between lasers and traditional dose rate testing techniques. However, the laser technique has not found a consistent, mainstream use for transient response outside of wafer screening, where the test setup has been calibrated to LINAC data and is tuned to a specific device or set of devices. This research illustrates that laser irradiation can provide similar data to the LINAC, but with the advantages that the laser is an affordable, laboratory-based, table-top system that provides repeatable data with a very high signal-to-noise ratio. Limiting the scope of the modeling application to discrete devices eliminates problems in characterization arising from metallization coverage and effects of multiple devices.

CHAPTER III

TEST SETUP

Devices

This study tests five common discrete devices. Three of the devices are general-purpose NPN transistors, the 2N3700 and two manufacturers' versions of the 2N2222 (referred to as *2N2222A* and *2N2222B*). The fourth device is a high-beta NPN transistor, the 2N2484. The last, which will be introduced later in the study, is an N-channel JFET, the 2N4391. All of these devices are readily available and often selected for systems usage as commercial-off-the-shelf (COTS) parts. All devices are packaged in a ceramic, leadless chip carrier (UB) package, enabling the same test circuitry to be used throughout the study.

The devices are tested with the base-emitter junction shorted and the base-collector junction reverse biased. Figure 3-1 shows the test circuit, which is used for both laser and LINAC testing. This test circuit is commonly used for testing at the NAVSEA Crane LINAC and was designed for flexibility to test a variety of devices. A Tektronix CT-2 current probe (1 mV/mA) is used to measure the current through the collector of the device under test (DUT) and the voltage at the collector is monitored for transients as well. The current probe is terminated with 50-Ohms while the voltage monitor is terminated with 1-MOhm. The ceramic capacitors used in this circuit are C1=4.7 μF, C2=4.7 μF, C3=1.0 μF, C4=1.0 μF, and C5=0.2 μF and are used for circuit stability and to control frequency response. The listed values reflect the total capacitance for the

“worst-case” part previously tested with this board configuration. Capacitance was not tuned specifically for these tests as the circuits were stable and performed as expected. The same board is used to test the JFET devices, which were biased with the gate-source junction shorted and the drain voltage and current were monitored.

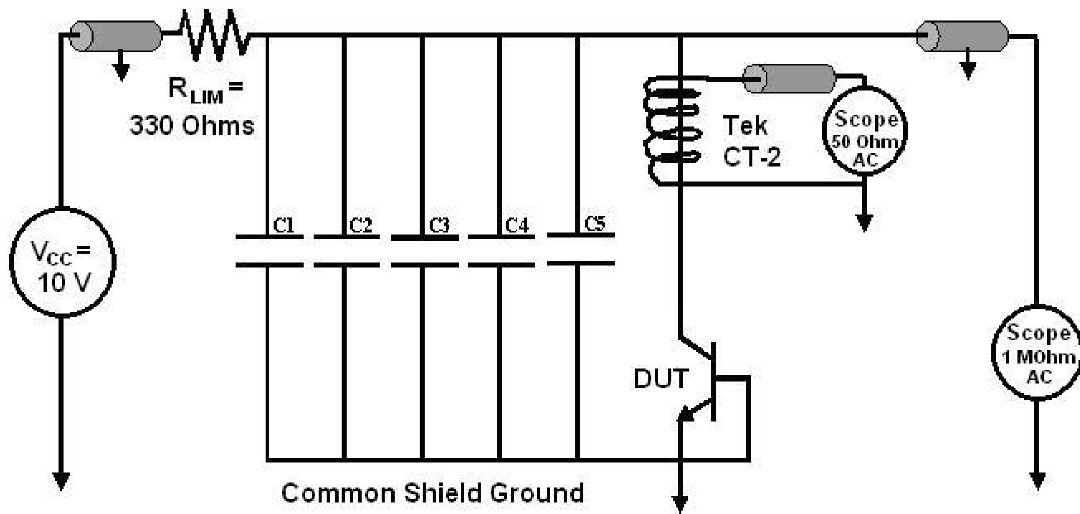

Figure 3-1: Schematic of device test board. The CT-2 probe measures current through the collector of the DUT and is terminated with 50 Ohms. V_{CC} indicates the bias voltage of 10 V throughout this study. The device under test (DUT), while represented as a BJT in this figure, represents other three-terminal devices such as MOSFETs or JFETs, which are biased in a similar way when using this test setup.

LINAC Testing

LINAC testing was performed at the NAVSEA Crane Linear Accelerator facility in Crane, Indiana in August 2007. The NAVSEA 40-pin I/O LINAC test fixture was used to perform this test (as seen in Figure 3-2). The test fixture is composed of two adjoining boxes designed to provide a Faraday cage around the test board. The larger box contains the necessary cabling and drivers. The smaller box contains the PIN diode for dosimetry,

a beam dump, and the test board. Lead bricks shield the larger cable box and an aluminum collimator is mounted to the faceplate to provide additional shielding. This procedure is described in [15].

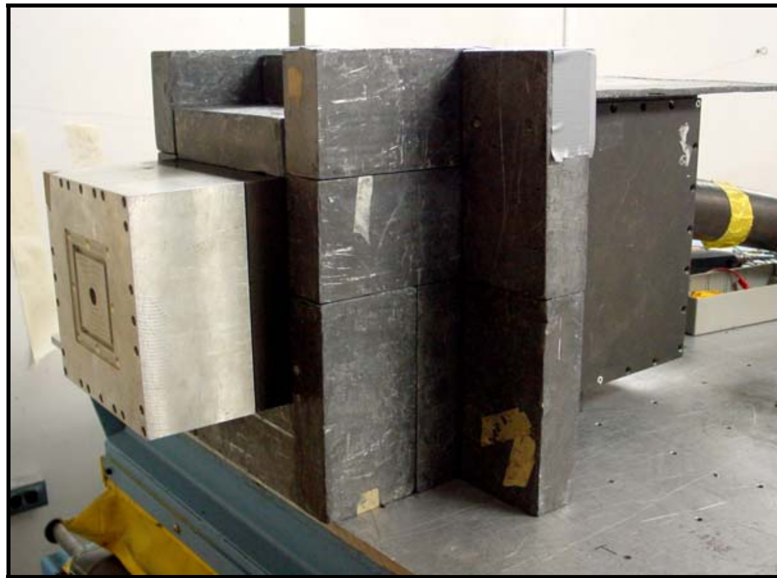

Figure 3-2: Photograph of LINAC 40 Pin I/O test fixture including lead bricks, and collimator (photo courtesy of NAVSEA Crane [15].)

Peak photocurrent response was determined using a radiation pulse width of approximately 200 nanoseconds (ns) at ambient room temperature. A range of dose rates from 10^8 to $4x10^{11}$ rad(Si)/s was used with the linear accelerator generating short bursts of 40 to 60 MeV electrons. The dose rates were achieved by changing the separation distance between the exit port and the DUT. A minimum of two parts of each device type were tested.

A typical LINAC shot profile, as monitored by the PIN diode, is shown in Figure 3-3. Resulting transient responses for a variety of radiation pulses in the four devices are shown in Figure 3-4. In all cases, the lowest dose rate induces the lowest response in the

device. For example, in the 2N2222A, a dose rate of 1.85 x 10^9 rad(Si)/sec produces the (nearly negligible) pulse while the pulse with a peak of approximately -0.5 A corresponds to a dose rate of 1.56 x 10^{10} rad(Si)/sec. An arrow indicates an increasing dose-rate response and the specific values are annotated on the individual graphs.

The specific dose-rate responses for individual shots at the LINAC facility are automatically calculated and recorded. In the case of this test, a pulse width of 200 ns was assumed and a dose-rate was calculated and displayed based on that assumption (see Figure 3-5). The automated data displays other information such as total ionizing dose effects and peak-to-peak measurements for each of the saved transients.

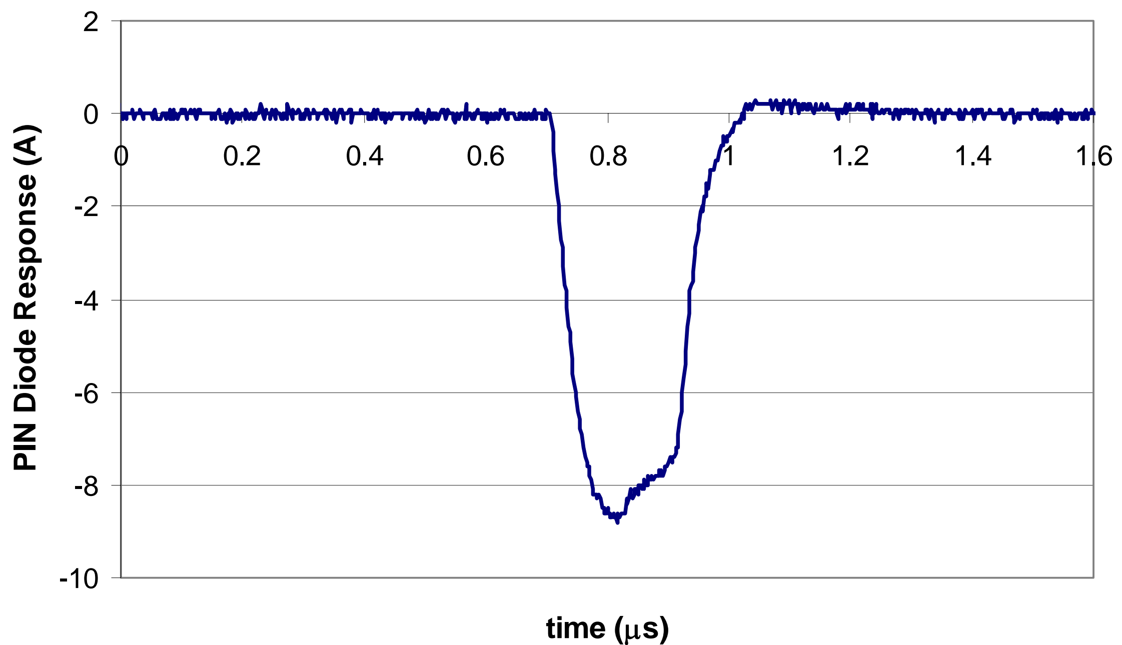

Figure 3-3: Monitor diode response of typical LINAC pulse at 1.9 x 10^9 rad(Si)/sec.

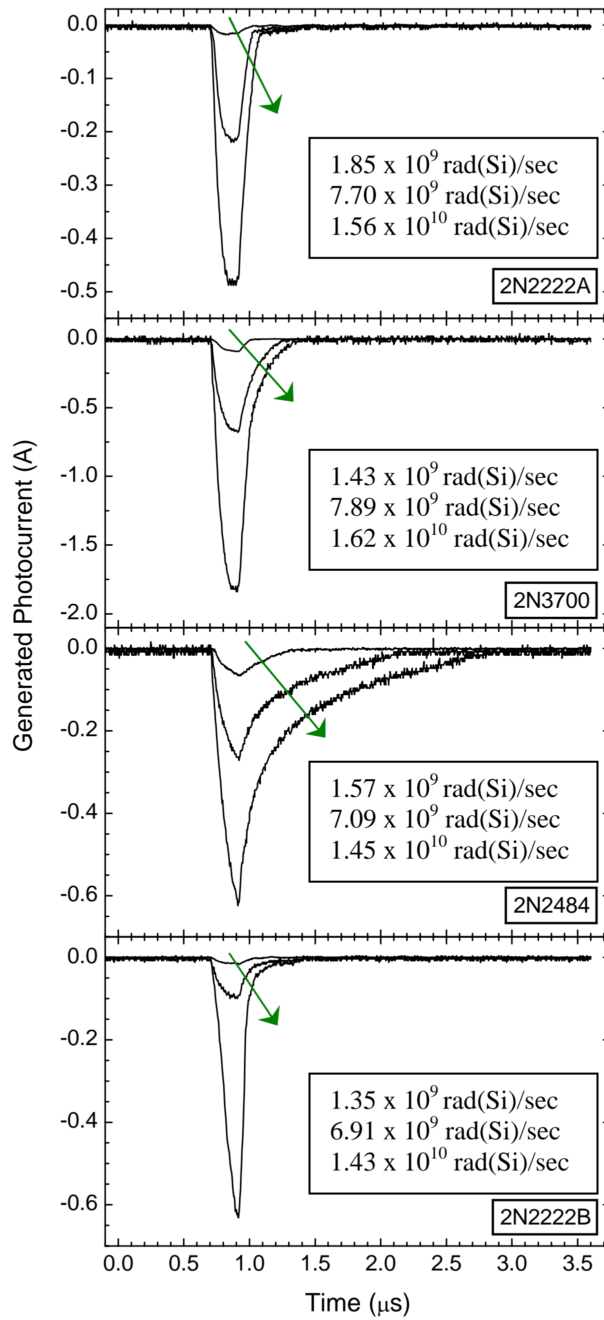

Figure 3-4: Resulting photocurrent transient responses from the LINAC for each of the devices. Arrows indicate increasing dose rates and the text boxes indicate the specific dose rates from low-to-high.

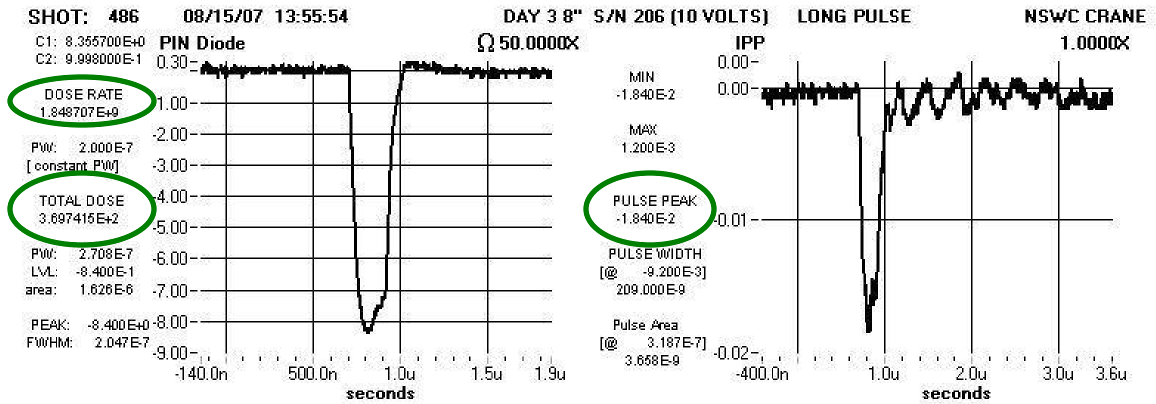

Figure 3-5: Automatically generated LINAC transients of the PIN diode and the photocurrent of the device output. This graph indicates dose rate (1.85 x 10^9 rad(Si)/sec) of the radiation pulse, peak current response generated by the pulse (18.4 mA), and total dose absorbed by the device (370 rad(Si)).

Laser Testing

A minimum of two parts of each of these device types were tested at the Naval Research Laboratory Laser laboratory in August 2007. The laser test was performed with an intracavity doubled, Q-switched Nd:YAG laser with a wavelength of 532 nm (2.33 eV) using a repetition rate of 1 kHz and a pulse width of approximately 200 ns. A diagram of the laser setup is shown in Figure 3-6. Test conditions from the LINAC were replicated where possible (i.e. the same test board was used, represented in the figure as the DUT). The laser spot was optimized at each test condition to produce the largest peak amplitude. At this optimized position, through a lens with a 12.5 cm focal length, the laser spot covered the die area and had a Gaussian characteristic.

The devices were exposed to a series of pulses while varying the laser power with the device biased at 10 V. To achieve continuous adjustment of the pulse energy, a polarizer-waveplate combination is employed. First, a half-waveplate is used to “rotate” the polarization of the beam. Then, the adjusted beam then encounters a polarizer. When

the polarization axis of the laser pulse is adjusted to be parallel to that of the polarizer, it experiences maximum transmission; when the two are orthogonal, maximum extinction occurs; in between, the transmission is continuously adjustable.

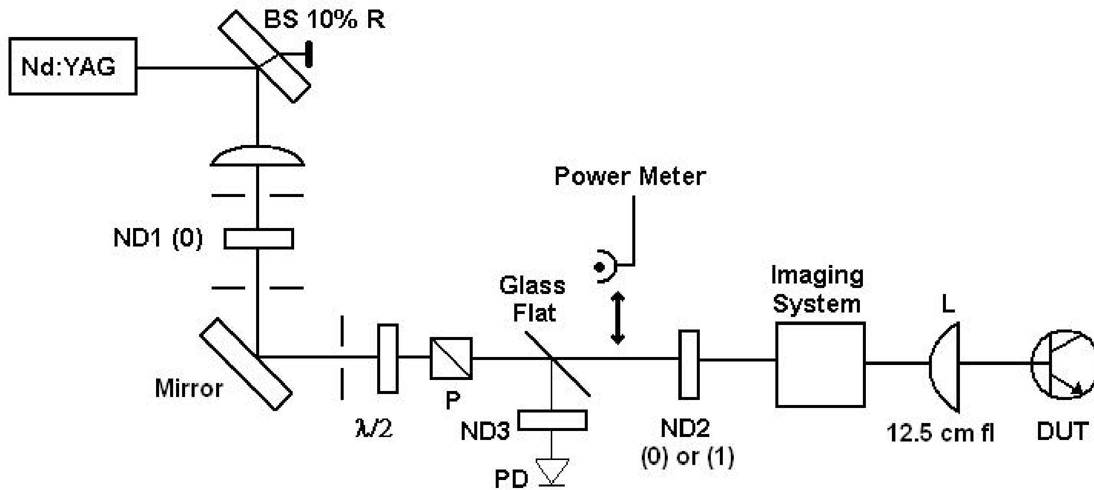

Figure 3-6: Diagram of Laser Setup (BS-beam splitter; ND-neutral density filter; λ/2-half-waveplate; P-polarizer; PD-photodiode; l-lens; fl-focal length; DUT-device under test). The test board from Figure 3-1 is the DUT.

Laser pulse energy (PE) was monitored for each data point using a calibrated photodiode. A typical transient, as monitored by this diode, is shown in Figure 3-7. The peak-to-peak output voltage of the photodiode was calibrated using a Laser Probe RK-3100 power meter inserted as shown in Figure 3-6, and scaled to represent the power incident on the device. Resulting transient responses for a variety of incident laser pulses in the four devices are shown in Figure 3-8. Again, in all cases, the lowest pulse energy induces the lowest response in the device. An arrow indicates an increasing photocurrent response and the specific values are annotated on the individual graphs.

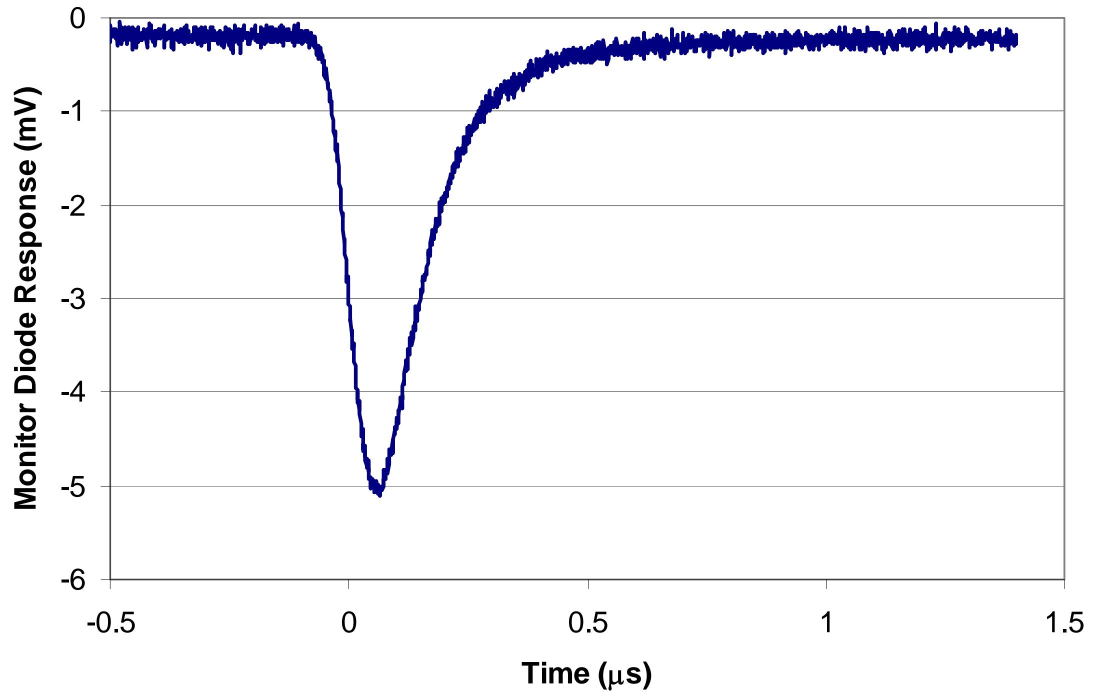

Figure 3-7: Monitor diode response of typical laser pulse

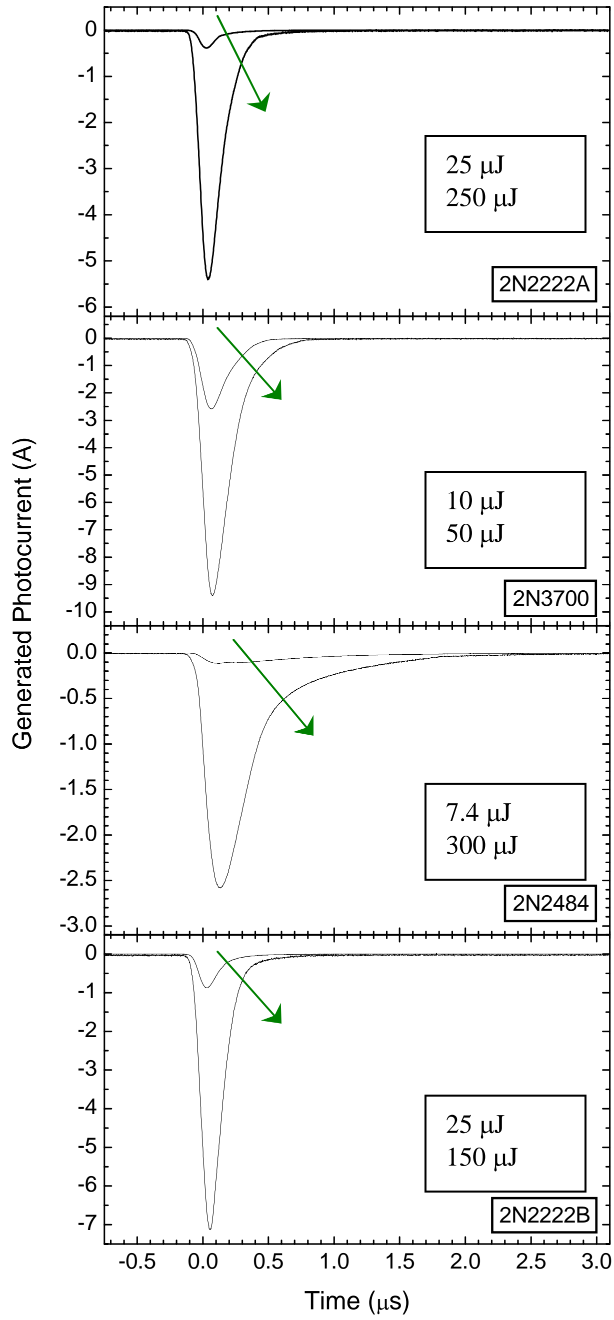

Figure 3-8: Resulting photocurrent transient responses from laser testing for each of the devices

CHAPTER IV

RESULTS

Conversion Factor and Combined Results

A complete set of LINAC I_{pp} data for the four device types is shown in Figure 4-1. The data points are single-shot results as recorded with the automated measurement system as described in the Test Setup chapter. K_{pp} values were extracted from these graphs using the linear fitting function (least-squares) in Microsoft Excel.

Figure 4-2 shows the corresponding data collected from the pulsed laser testing. These data are individual data points as indicated by the peak-to-peak data from the oscilloscope. As in the LINAC data, the K_{pp} values for the laser data have been extracted from these graphs using the least-squares linear extraction in Excel. The K_{pp} values for both LINAC and laser data are summarized later in this chapter.

The dynamic range of the laser facility is significantly larger than that utilized in this study. Based on these data and the capabilities of the laser facility, dose rates lower than 10^{9} rad(Si)·sec^{-1} and greater than 10^{12} rad(Si)·sec^{-1} are readily available, if desired. This is significant because the accelerator facilities capable of consistently delivering dose-rate levels above 10^{12} rad(Si)·sec^{-1} tend to be prohibitively expensive for the extensive testing that is desired for model extraction. The modeling technique described in this project projects the linear portion of the I_{pp} vs. dose-rate curve beyond the "roll-off," as described in the Background chapter. Having high dose rate data readily available will make it possible to more accurately characterize the devices.

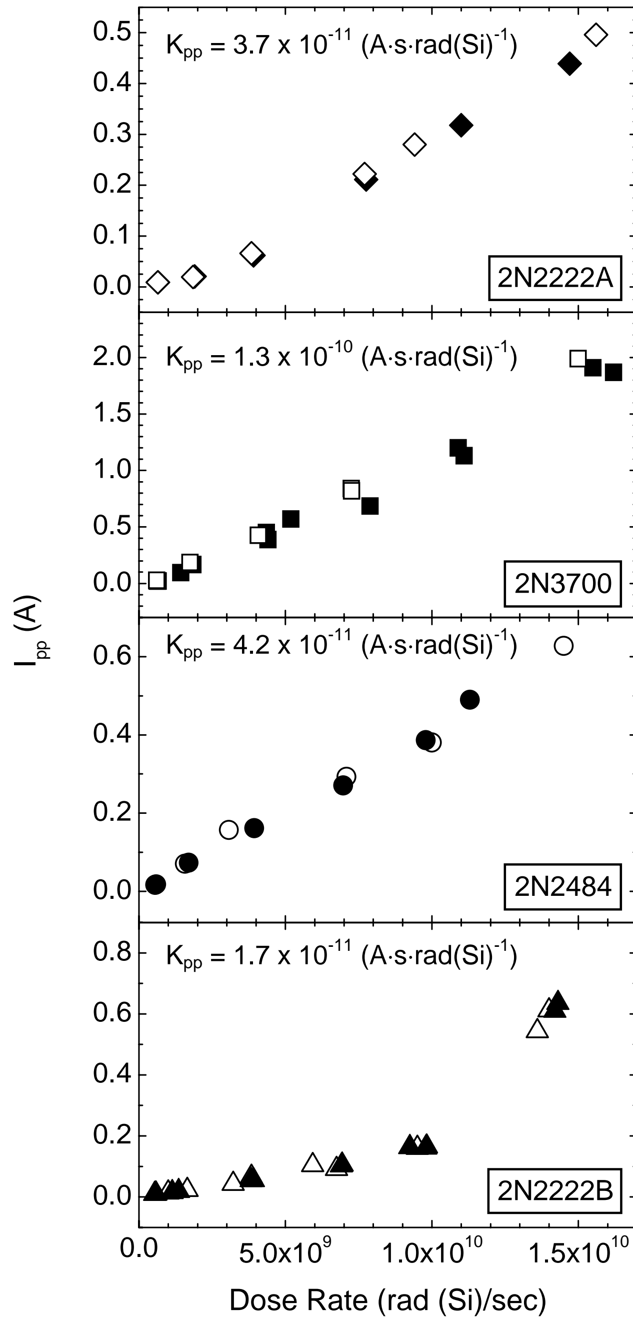

Figure 4-1: LINAC I_{pp} vs. dose rate for each of the tested device types. Two devices of each type were tested. Solid and hollow symbols represent data from individual devices.

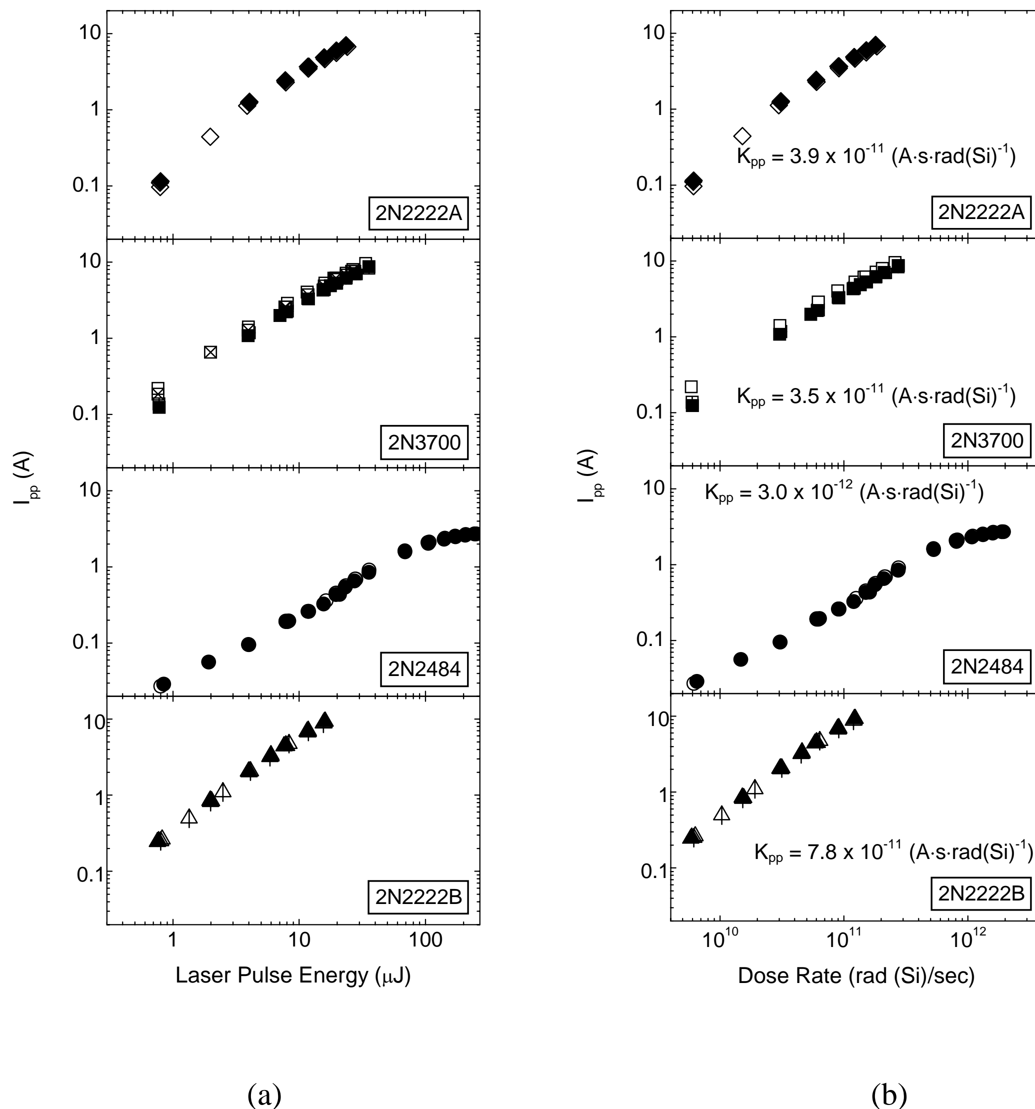

Figure 4-2: Laser I_{pp} data for each of the four tested device types plotted as I_{pp} vs. pulse energy (a) and I_{pp} vs. dose rate (b). Different symbol types, solid, hollow, and hashed (if necessary), represent data for different tested devices. There are 2-3 devices tested for each part type.

In order to directly compare the laser and LINAC data, it is necessary to convert laser PE to an equivalent dose rate. This is accomplished by selecting matching (within

5%) I_{pp} data points from laser and LINAC data sets. The LINAC dose rate value is divided by the pulse energy at each of those points. The conversion factor (CF) is the resulting average of the pulse-energy-to-dose-rate quotients:

$$DR = PE \cdot CF \qquad (4.1)$$

In this equation, DR is dose-rate (rad(Si)·sec^{-1}), PE is the pulse energy (μJ), and CF is the conversion factor (rad(Si)·sec^{-1}·μJ^{-1}). The CF value is then applied to the entire data set to convert to dose rate. Figure 4-3 illustrates the process with the 2N3700 device data.

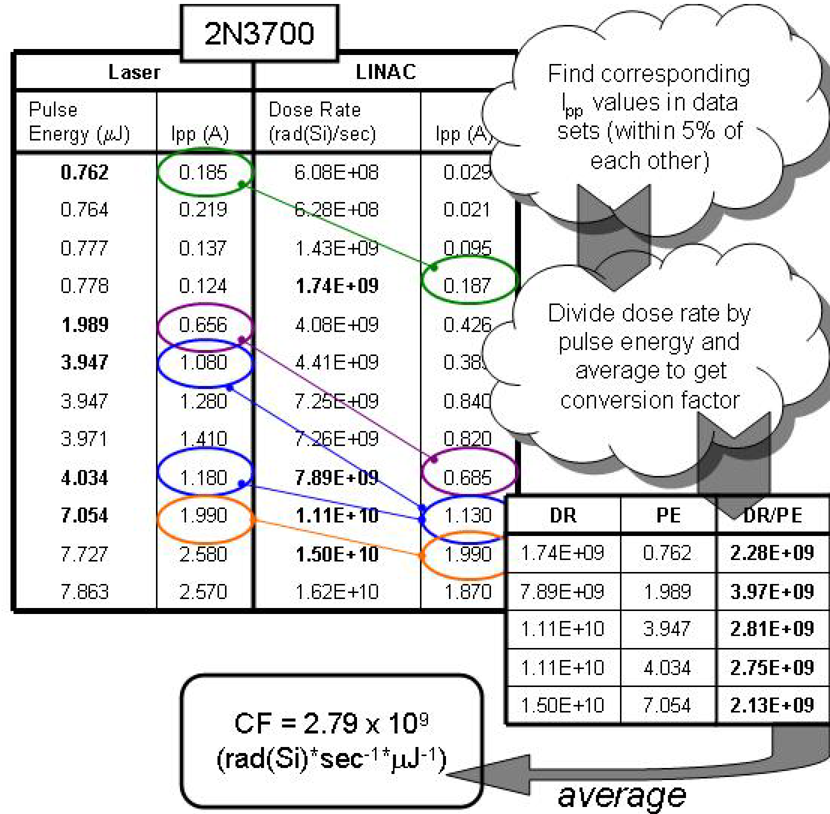

Figure 4-3: Procedure for extraction of CF from LINAC and laser data illustrated using data taken for the 2N3700.

Each device type is found to have a different CF; Table 4-1 summarizes these values. A practical illustration of the differing CFs comes from comparing the data sets in Figures 4-4 (a and b). The four graphs in Figure 4-2a and 4-2b have been combined to form Figures 4-4 (a and b), respectively. The laser measurements for each of the different device types were performed over the same pulse energy range, with the 2N2222B exhibiting the highest I_{pp} values over this range and the 2N2484 exhibits the lowest (Fig. 4-4a). When the data are converted to dose rate, the 2N3700 exhibits the highest I_{pp} with respect to dose rate and the 2N2222A exhibits the lowest at dose rates below 8×10^{10} rad(Si)·sec^{-1} (Fig. 4-4b).

Table 4-1: Summary of CF data—values are extracted as illustrated in Figure 4-3.

Device Type	CF (rad(Si)·sec^{-1}·μJ^{-1})
2N2222A	7.68×10^{9}
2N3700	2.79×10^{9}
2N2484	5.69×10^{8}
2N2222B	8.80×10^{9}

The combined laser and LINAC I_{pp} data are shown in Figure 4-5 (a combination of Figures 4-1 and 4-2b). Laser data, using the converted dose rate (solid symbols), fall into the general trend lines established from the LINAC data (hollow symbols) for all device types. Table 4-2 shows a comparison of K_{pp} values extracted from laser and LINAC data as well as a calculated value based on what is known from the device geometries. This table illustrates the variation in K_{pp} values based on the extraction method. All of the values are considered acceptable for model creation. Because the LINAC provides events closest to that of the weapons environment, the LINAC should

give the most accurate value for K_{pp}. However, the noise associated with LINAC data brings into question the true validity of the LINAC-extracted K_{pp} value. It should be noted that the laser data in Figure 4-5 indicates a much tighter grouping within the devices as compared to the LINAC data.

Table 4-2: K_{pp} device values extracted from laser and LINAC data

Device Type	LINAC K_{pp} (A·s·rad(Si)$^{-1}$)	Laser K_{pp} (A·s·rad(Si)$^{-1}$)	Calculated K_{pp} (A·s·rad(Si)$^{-1}$)
2N2222A	3.71×10^{-11}	3.87×10^{-11}	9.62×10^{-12}
2N3700	1.31×10^{-10}	3.50×10^{-11}	1.18×10^{-11}
2N2484	4.17×10^{-11}	2.96×10^{-12}	5.75×10^{-12}
2N2222B	1.74×10^{-11}	7.78×10^{-11}	7.17×10^{-12}

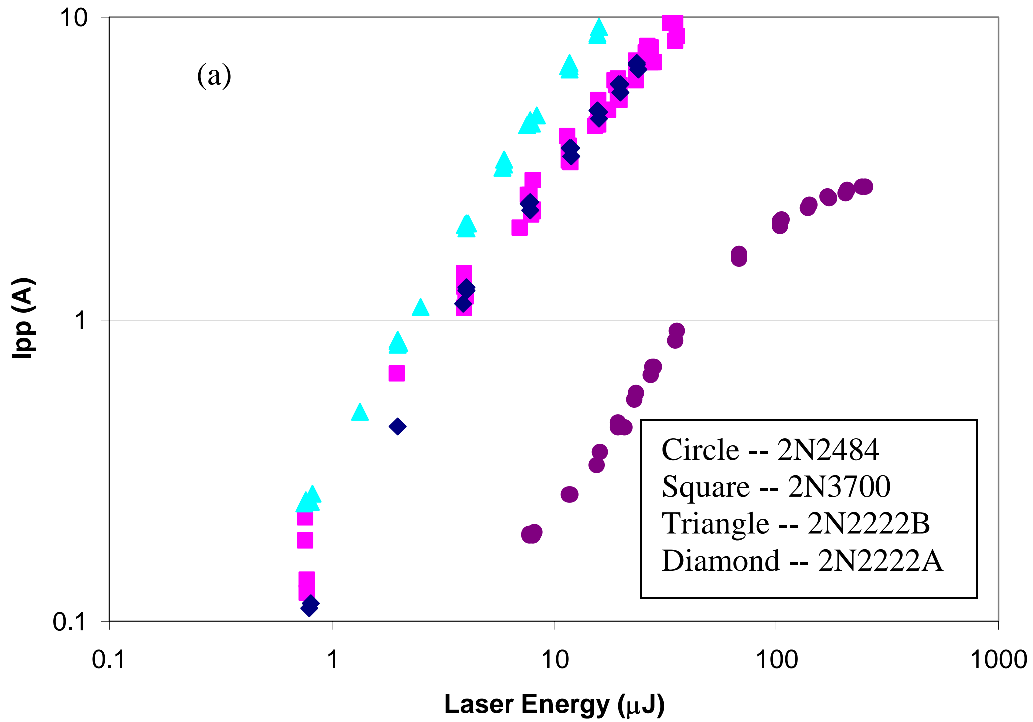

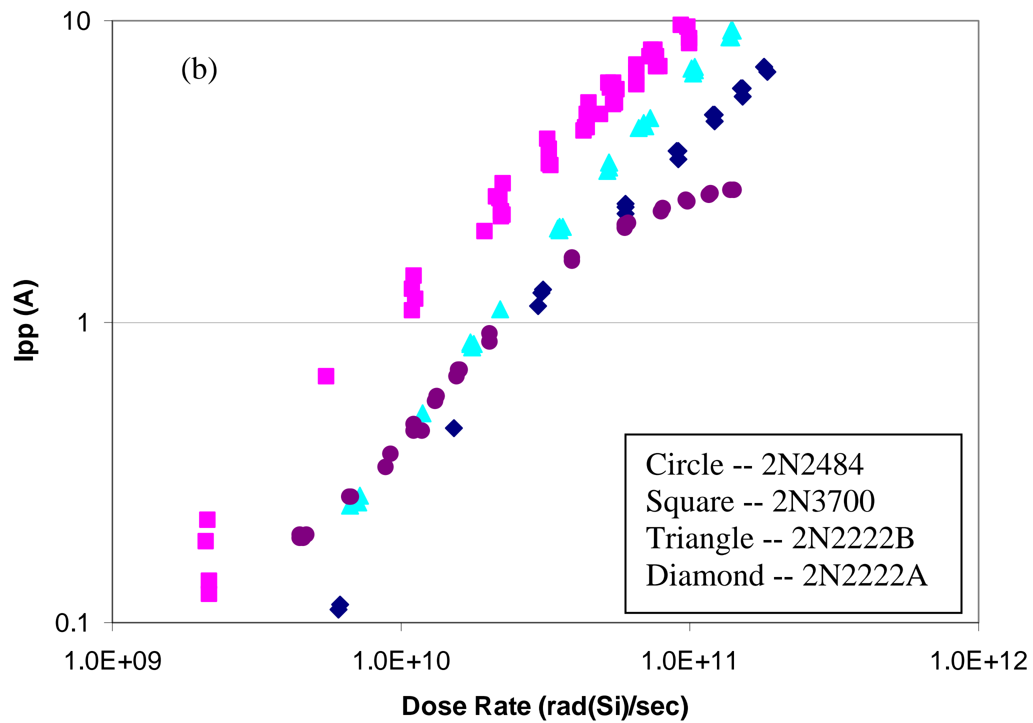

Figure 4-4: Device-type relationship shift when CF is applied. All laser I_{pp} vs. laser energy data (a) and I_{pp} vs. dose rate laser data (b). Note the differences in series order from left-to-right in the two graphs.

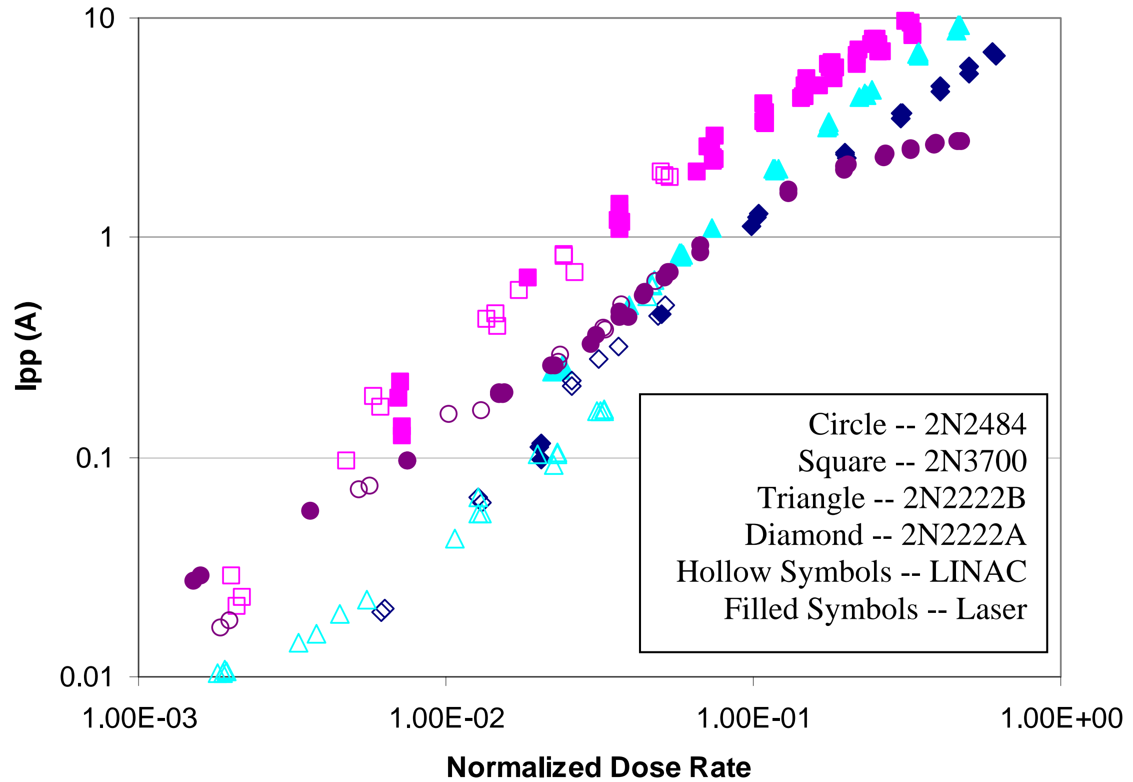

Figure 4-5: Combined LINAC and laser I_{pp} data (hollow symbols—LINAC, solid symbols—laser). Both data sets are based on approximately 200 ns pulses from respective sources.

Accounting for Metallization Coverage

Previous work on this topic has identified and attempted to address issues with metallization coverage [12-14]. Unlike the LINAC, the laser pulse does not penetrate the metal coverage of the die and does not illuminate the active area directly under areas of metallization as demonstrated in Figure 4-6, a simplified diagram of shadowing effects. The figure does not show the nuance complexities of light "bending" around metallization. Details regarding shadowing and intensity have been explored further in [14] and do not have a significant impact on this discussion of discrete part modeling.

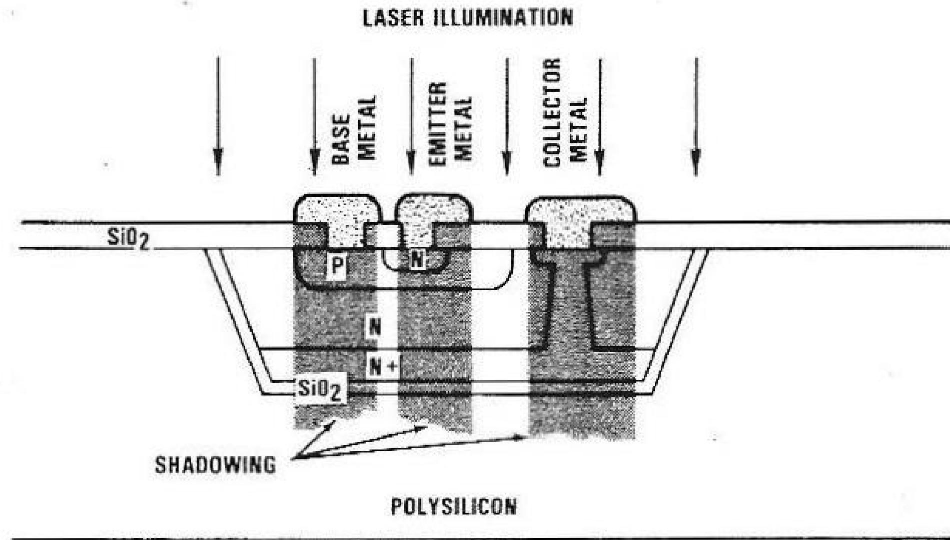

Figure 4-6: Laser irradiation and shadowing of a typical bipolar transistor cross section. Figure from King [11].

The difference in metallization patterns in different die contributes to the different CF among parts. Metallization patterns effectively reduce the die area when doing laser testing. Therefore, for a heavily metallized device, more energy from the laser will be required to generate the same amount of photocurrent than that for a less covered device.

This additional energy is quantifiable because generated photocurrent is based on device geometry and dose rate. The CF for each device directly relates the laser pulse energy to a dose rate. If there was no metallization, devices with similar geometries should require similar laser pulse energies to generate the same photocurrent found in LINAC testing. For example, three of the tested devices in this study have very similar geometries, the 2N2222A, 2N2222B, and the 2N3700, yet these devices have different CFs (see Table 4-1).

A relationship between the metal coverage and CF was established using an image processing technique on photomicrographs of the dice in question. The

photographs were scanned and cropped to include only the active area. Then, a thresholding algorithm, as well as some morphological operations, was used to obtain a monochromatic image to determine the metal and non-metal areas of the die.

For example, Figure 4-7 shows a sample die photo with a corresponding processed image for the 2N2222. The algorithm first converts the image to a grayscale image, then the image is smoothed to average out slight variations in large areas such as the patterns in the metallization. Next, a threshold is set to filter hues and assign individual pixels to either black or white to create a two-toned image; in this case, the mid-tones and darker are considered active area and are filtered to black and mid-tones and lighter are considered metal and are filtered to white. The resulting figure is then refined by hand to best match the metal coverage and compared to the original die photo. This is necessary due to abnormalities in the die photo and issues with the bond wire areas. Using the pixel ratio of this image, the percentage of metal is established. Table 4-2 shows metal coverages extracted from the thresholding technique for the tested devices and reiterates the CF for each of the devices. Metal coverage information is also shown for the 2N4391, which is discussed later in this chapter.

Table 4-3: Percent metal coverage results of thresholding technique and summary of CFs from Table 4-1 (**includes JFET device metal coverage for later discussion)

Device Type	CF (rad(Si)·sec^{-1}·µJ^{-1})	Percent Metal Coverage
2N2222A	7.68×10^{9}	54
2N3700	2.79×10^{9}	77
2N2484	5.69×10^{8}	85
2N2222B	8.80×10^{9}	39
2N4391	**	39

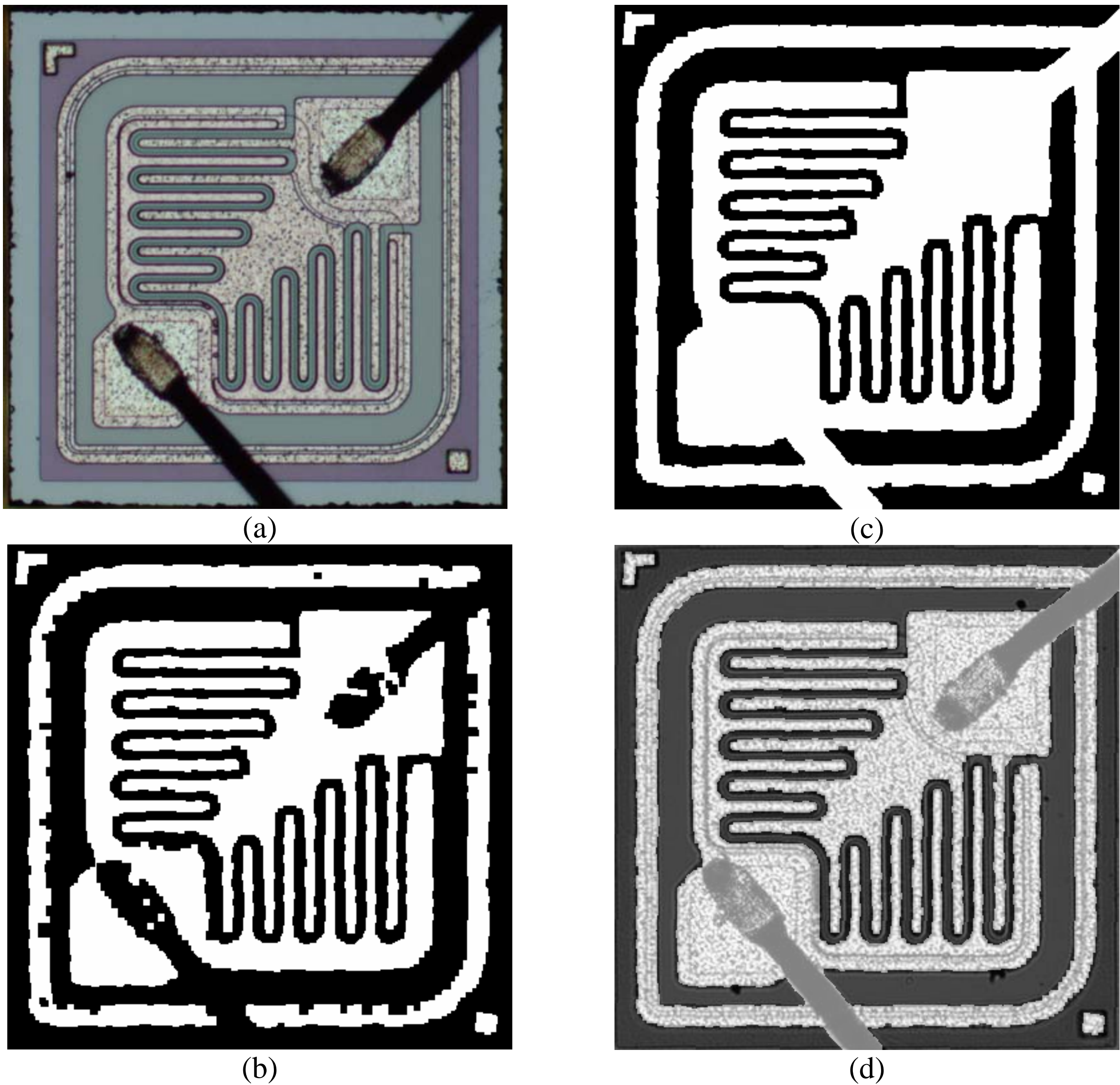

Figure 4-7: Thresholding technique progression for the 2N2222A (a) original die photo (b) monochromatic image (c) hand-corrected monochromatic image and (d) direct overlay with die photo.

The CF determined in the first part of this chapter for each part type is plotted vs. the percent metal coverage in Figure 4-8 (a visualization of the data in Table 4-3). This plot strongly suggests a linear relationship between the percent of active area covered by metal and the CF for the individual devices. A linear least-square fit was done for the data points for the 2N2222A, 2N2222B, and 2N3700 devices and the extrapolated line is

indicated in the figure.

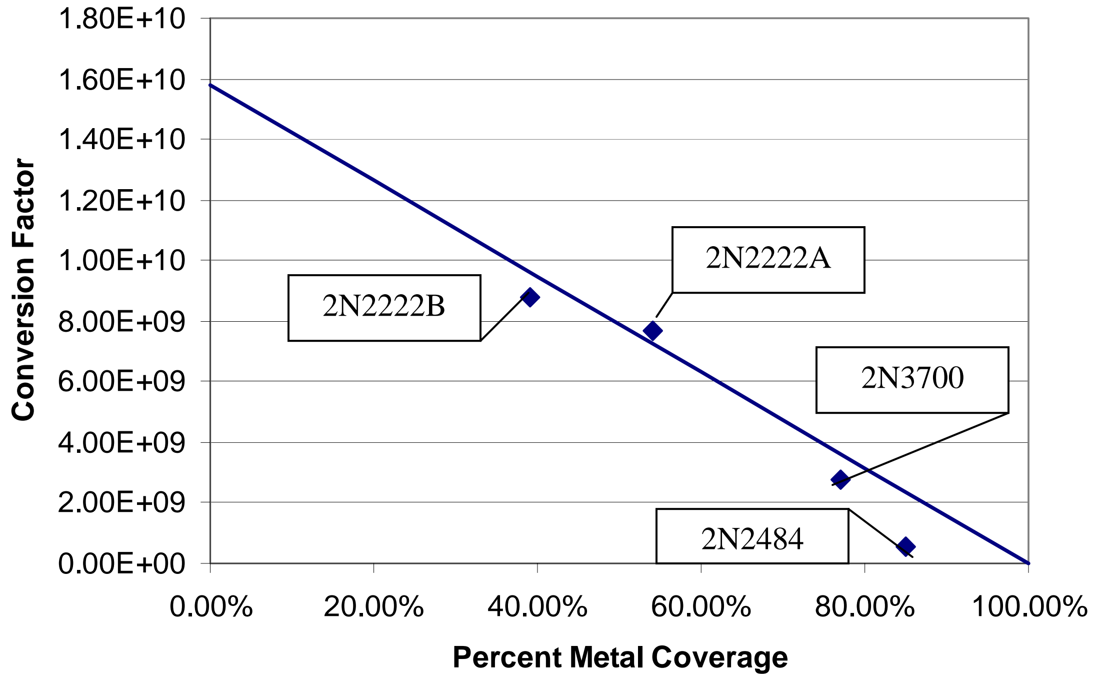

Figure 4-8: Conversion factor vs. percent metal coverage

The implication of this linear extrapolation is that a CF can be determined solely by the percent metal coverage of a device, which can then be used to determine the equivalent dose-rate without validation with LINAC data. This process will be valid only for devices with similar geometries. CF vs. metal coverage is also plotted for the 2N2484 in Figure 4-8. This device does not fall on the line established by the other devices because it has a significantly different geometry; the collection region is about twice as deep and the die size is about half of the others.

Another indication of this geometrical difference is seen in Figure 4-9, a reiteration of Figure 4-5, laser I_{pp} vs. pulse energy. The figure includes an additional set

of data taken for a JFET device, the 8CLJQ045. This device has no corresponding LINAC data and thus was not included earlier in this study. It is clear that the response to laser pulse energy is significantly different for the 2N2484 and the 8CLJQ045 than the other devices. Theoretically, devices with a similar geometry to the 2N2484 or the 8CLJQ045 will form individual groupings similar to that of the 2N2222A, 2N2222B, and 2N3700. However, no data have been taken to establish this as fact.

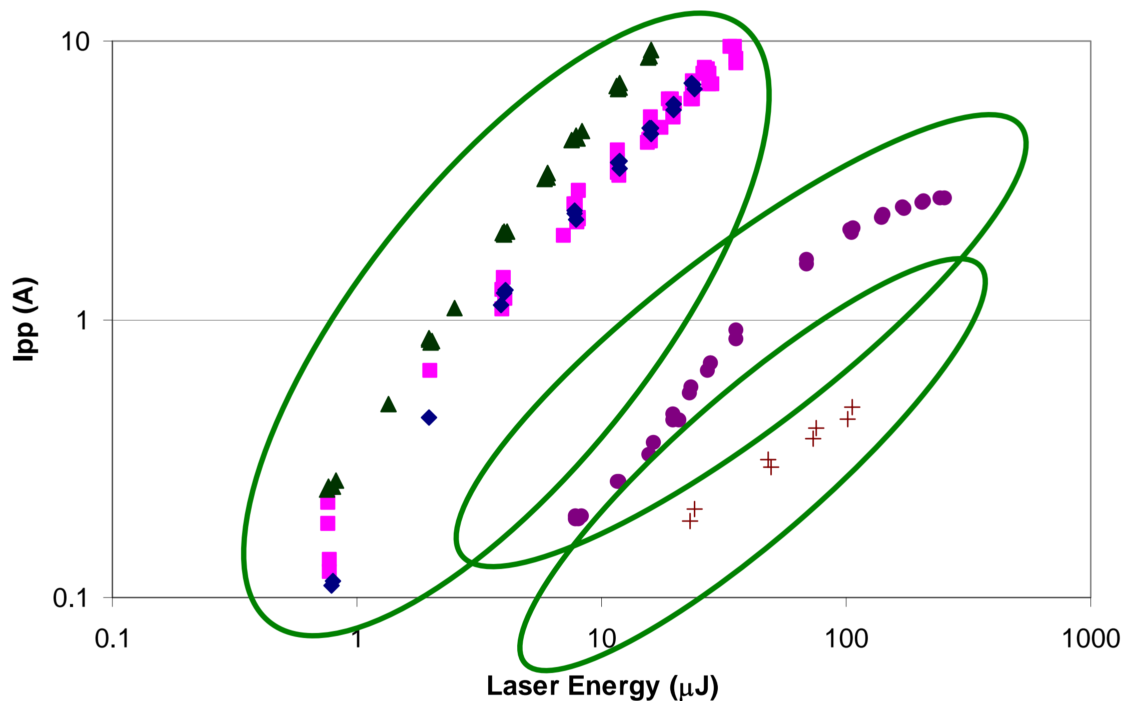

Figure 4-9: Geometry family groupings from laser data. From left to right: both 2N2222 devices (blue diamonds and green triangles) grouped with the 2N3700 (fuchsia squares), the 2N2484 (purple circles), and finally, the 8CLJQ045 (brown plus-signs).

In order to fully establish a procedure to determine CF without correlation with LINAC data, it would be necessary to characterize a wide variety of device geometry families that provide general groupings as mentioned above. For each of these geometry

families, a CF vs. metal coverage line would need to be established. One could then establish a geometry family, determine the percent metal coverage, and look up the CF for any discrete device and create a dose-rate model based on this information.

Case Study of the 2N4391

To utilize this technique for an unknown part, one must first establish the geometry family of the device and the metal coverage of the die. An example is provided using the 2N4391 JFET device. Raw laser data was found to be in the same general grouping as the 2N3700, 2N2222A, and 2N2222B, as seen in Figure 4-10, so Figure 4-8 is the correct CF vs. percent metal coverage curve to use. The metal coverage is listed in Table 4-3 to be 39%. One would then find the corresponding CF in Figure 4-8, which is 9.5 x 10^9 rad(Si)·sec^{-1}·μJ^{-1}. This CF can be applied directly to the value of the slope extracted from the laser I_{pp} data or, the I_{pp} vs. laser energy data can be converted to I_{pp} vs. dose-rate and then extract the K_{pp}. These two techniques yield the same result. Applying the CF directly to the K_{pp} value is significantly more direct, but the conversion to an equivalent dose rate is necessary for comparison to LINAC data and is therefore shown in the process below. Figure 4-10 shows the flow for this procedure in image form.

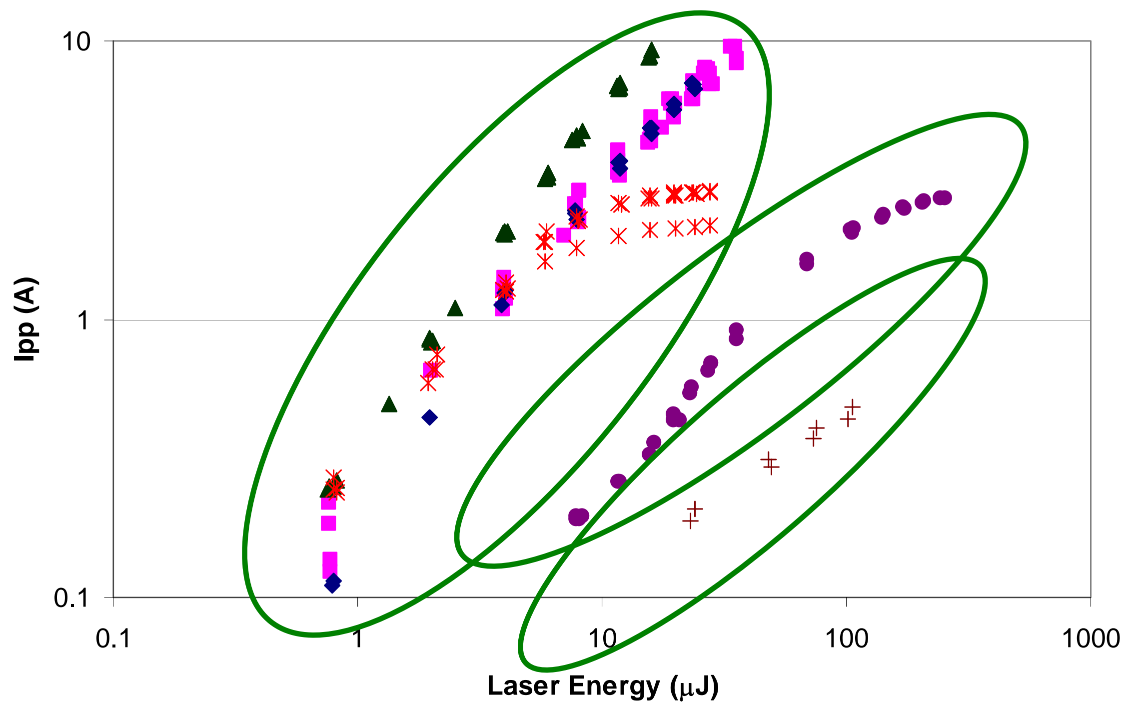

Figure 4-10: Establishment of device geometry family using acquired laser data. The 2N4391 (red stars) falls into the classification with the 2N2222A, 2N2222B, and 2N3700.

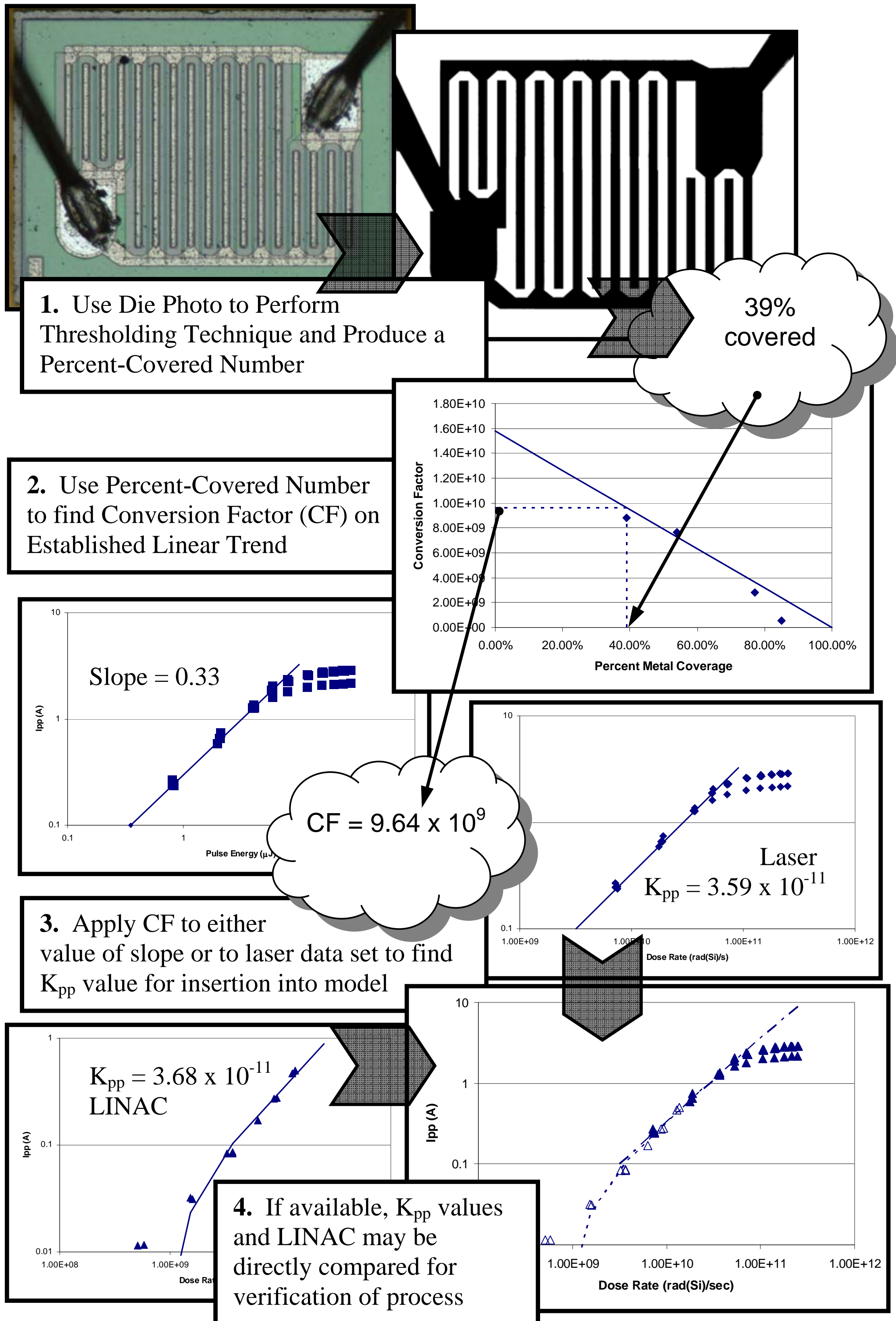

Figure 4-11: Process flow using the 2N4391

CHAPTER V

CONCLUSIONS

The use of a pulsed laser to produce dose rate data provides a low-cost, table-top alternative to a LINAC facility. A highly-reliable laser can be commercially purchased and a test set-up to perform this testing for extracting modeling information can be set up in almost any laboratory setting. No special training or certification is necessary to operate a laser such as this and there is no radiation hazard. The laser approach provides high signal-to-noise ratio data with signals that can be easily replicated into a SPICE-like environment for model verification. The data taken from the laser is highly reproducible.

Preliminary results from this study were presented at the Hardened Electronics and Radiation Technologies (HEART) Conference in March 2007. From this, interest was generated for this technique in the area of nuclear event detector (NED) device testing. It has also been suggested that, for small integrated circuits (ICs), a pulsed laser could be used to verify macro-models.

The use of a pulsed laser to produce a dose-rate response has long been established. However, the issues with metallization coverage have prevented a mainstream application beyond simple threshold testing at fabrication facilities. These applications are generally tuned specifically to a single device type and are calibrated with LINAC data, providing little flexibility to the process. The linear relationship between percent metal coverage and conversion factor provides a very good estimate on equivalent dose rate and makes possible a very reasonable alternative to LINAC testing

for model creation.   By limiting the application to modeling purposes, device evaluation testing (DET) and qualification testing is left to be done at a LINAC facility without interruptions for model development.

The results discussed in this study are intentionally limited to the modeling application. This is not a suggestion that dose rate laser testing could replace LINAC or flash x-ray testing entirely, however, real advantages exist for the specific application of model development and evaluation: the laser data is repeatable, with a known pulse shape over a large dynamic range with no long-term radiation damage to the tested devices.

The primary outcome of this research is to establish a way to correlate laser pulse energy results to an equivalent dose rate value without having to use a LINAC to validate the data. It is demonstrated that laser dose rate data can be converted to equivalent LINAC data and that the percent coverage of metallization has a linear relationship with the conversion factor of individual devices based on device geometry. By establishing the device-geometry family and using the percent metal coverage of the active area of the die, the corresponding conversion factor can be determined from a figure showing this relationship and can be applied to the laser data to establish dose rate or may be applied directly to the slope of the laser data to establish the correlating K_{pp} for insertion into dose-rate models. This process can be performed using a common laser and may be quickly applied to produce models for the ever-changing discrete-parts lists for weapons system development.

REFERENCES

[1] J.L. Wirth and S.C. Rogers, "The transient response of transistors and diodes to ionizing radiation," *IEEE Trans. Nucl. Sci*., pp. 24-38, November 1964.

[2] E.W. Enlow and D.R. Alexander, "Photocurrent Modeling of Modern Microcircuit PN Junctions," *IEEE Trans. Nucl. Sci*., vol. 35, no. 6, pp. 1467-1474, December 1988.

[3] D.R. Alexander, "Transient Ionizing Radiaiton Effects in Devices and Circuits," *IEEE Trans. Nucl. Sci*., vol. NS-50, no. 3, pp. 565-582, June 2003.

[4] A. Holmes-Seidle and L. Adams, Handbook of Radiation Effects, Second Edition, New York, Oxford University Press: 2002

[5] D.H. Habing, "The Use of Lasers to Simulate Radiation-Induced Transients in Semiconductor Devices and Circuits," *IEEE Trans. Nucl. Sci.*, vol. NS-12, pp. 91-100, October 1965.

[6] T.D. Ellis and Y.D. Kim, "Use of a pulsed laser as an aid to transient upset testing of I^2L LSI Microcircuits," *IEEE Trans. Nucl. Sci.*, vol. NS-25, no. 6, pp. 1489-1493, December 1978.

[7] M.N. Hardman and A.R. Edwards, "Exploitation of a Pulsed Laser to Explore Transient Effects on Semiconductor Devices", *IEEE Trans. Nucl. Sci.*, vol. NS-31, no.6, pp. 1406-1410, December 1984.

[8] A.H. Johnston and M.P. Baze, "Mechanisms for the Latchup Window Effect in Integrated Circuits," *IEEE Trans. Nucl. Sci.*, vol. NS-32, no. 6, pp. 4018-4025, December 1985.

[9] W.D. Raburn, S.P. Buchner, K. Kang, R. Singh, and S. Sayers, "Comparison of Threshold Transient Upset Levels Induced by Flash X-Rays and Pulsed Lasers", *IEEE Trans. Nucl. Sci.,* vol. NS-35, no.6, pp. 1512 - 1516, December 1988.

[10] A.I. Chumakov, A.N. Egorov, O.B. Mavritsky, A.Y. Nikiforov, A.V. Yanenko, "Single Event Latchup Threshold Estimation Based on Laser Dose Rate Test Results," *IEEE Trans. Nucl. Sci*., vol. 44, no. 6, pp. 2034-2039, December 1997

[11] E.E. King, B. Ahlport, G. Tettemer, K. Mulker, and P. Linderman, "Transient Radiation Screening of Silicon Devices Using Backside Laser Irradiation," *IEEE Trans. Nucl. Sci.*, vol. NS-29, no.6, pp. 1809-1815, December 1982

[12] P.K. Skorobogatov, A.Y. Nikiforov, A.A. Demidov, "A Way to Improve Dose Rate Laser Simulation Adequacy," *IEEE Trans. Nucl. Sci*., vol. 45, no. 6, pp. 2659-2664, December 1998

[13] A.H. Johnston, M.P. Baze, "Experimental Methods for Determining Latchup Paths in Integrated Circuits," *IEEE Trans. Nucl. Sci*., vol. NS-32, no. 6, pp. 4260-4265, December 1985

[14] A.Y. Nikiforov, P.K. Skorobogatov, "Dose Rate Laser Simulation Test Adequacy: Shadowing and High Intensity Effects Analysis," *IEEE Trans. Nucl. Sci.*, vol. 43, no. 6, pp. 3115-3121, December 1996

[15] J.L Titus, Quick Look Test Report (Transient and Survivability), Report, NAVSEA Crane, Dec. 2004